Downloaded from jnm.snmjournals.org by on March 15, 2017. For personal use only.

Evaluation of 3D Monte Carlo–Based Scatter Correction for ^{201}Tl Cardiac Perfusion SPECT

Jianbin Xiao[1,2], Tim C. de Wit[1,2], Wojciech Zbijewski[1,2], Steven G. Staelens[3], and Freek J. Beekman[1,2]

[1]*Department of Nuclear Medicine, Image Sciences Institute, University Medical Centre Utrecht, Utrecht, The Netherlands;* [2]*Department of Pharmacology and Anatomy, Rudolf Magnus Institute of Neuroscience, University Medical Centre Utrecht, Utrecht, The Netherlands; and* [3]*Department of Medical Imaging and Signal Processing, Ghent University, Ghent, Belgium*

^{201}Tl-Chloride (^{201}Tl) is a myocardial perfusion SPECT agent with excellent biochemical properties commonly used for assessing tissue viability. However, cardiac ^{201}Tl SPECT images are severely degraded by photons scattered in the thorax. Accurate correction for this scatter is complicated by the nonuniform density and varied sizes of thoraxes, by the additional attenuation and scatter caused by female patients' breasts, and by the energy spectrum of ^{201}Tl. Monte Carlo simulation is a general and accurate method well suited to modeling this scatter. **Methods:** Statistical reconstruction that includes Monte Carlo modeling of scatter was compared with statistical reconstruction algorithms not corrected for scatter. In the ADS method, corrections for attenuation, detector response, and scatter (Monte Carlo–based) were implemented simultaneously via the dual-matrix ordered-subset expectation maximization algorithm with a Monte Carlo simulator as part of the forward projector. The ADS method was compared with the A method (ordered-subset expectation maximization with attenuation correction) and with the AD method (a method like the A method but with detector response modeling added). A dual-head SPECT system equipped with two ^{153}Gd scanning line sources was used for simultaneously acquiring transmission and emission data. Four clinically realistic phantom configurations (a large thorax and a small thorax, each with and without breasts) with a cardiac insert containing 2 cold defects were used to evaluate the proposed reconstruction algorithms. We compared the performance of the different algorithms in terms of noise properties, contrast-to-noise ratios, the contrast separability of perfusion defects, uniformity, and robustness to anatomic variations. **Results:** The ADS method provided images with clearly better visual defect contrast than did the other methods. The contrasts achieved with the ADS method were 10%–24% higher than those achieved with the AD method and 11%–37% higher than those achieved with the A method. For a typical contrast level, the ADS method exhibited noise levels around 27% lower than the AD method and 34% lower than the A method. Compared with the other 2 algorithms, the ADS reconstructions were less sensitive to anatomic variations and had better image uniformity in the homogeneously perfused myocardium. Finally, we found that the improvements that can be achieved with Monte Carlo–based scatter correction are stronger for ^{201}Tl than for ^{99m}Tc imaging. **Conclusion:** Our results indicate that Monte Carlo–based scatter correction is suitable for ^{201}Tl cardiac imaging and that such correction simultaneously improves several image-quality metrics.

Key Words: quantitative SPECT; cardiac imaging; scatter correction; Monte-Carlo simulation

J Nucl Med 2007; 48:637–644
DOI: 10.2967/jnumed.106.037259

Thallium-201 chloride (^{201}Tl) is a perfusion agent commonly used for myocardial perfusion SPECT. In addition to assessment of myocardial perfusion in both stress and rest situations, the unique redistribution property has made ^{201}Tl SPECT an effective modality for identifying myocardial viability (*1*). However, because of the combined effects of some of the physical properties of ^{201}Tl, the quality of SPECT images obtained with this perfusion agent is often suboptimal. Compared with ^{99m}Tc images, ^{201}Tl images are more degraded by attenuation and scatter because of the lower energy of the dominant ^{201}Tl x-ray photopeak. Furthermore, dosimetric considerations related to the long physical half-life of ^{201}Tl restrict the allowed myocardial activity to levels as much as 4 times lower than typical ^{99m}Tc concentrations. These factors together result in a significantly higher noise level and lower quantitative accuracy for the reconstructed ^{201}Tl images than for the ^{99m}Tc images. Despite the ongoing debate as to whether ^{99m}Tc-labeled perfusion agents should or could replace ^{201}Tl for myocardial perfusion SPECT studies, the latter still is often used in clinical practice. According to a report (*2*), approximately 60% of the cardiac SPECT studies performed yearly in the United States in the late 1990s used ^{201}Tl. A similar usage of ^{201}Tl was also found by a more recent survey conducted in the United Kingdom (*3*). Therefore, improving the image quality for ^{201}Tl cardiac SPECT remains clinically important.

Among all the image-degrading factors present in the cardiac SPECT studies, attenuation, collimator and detector blurring, and scatter have a large impact on the quantitative accuracy and the clinical diagnosis. Several experiments have shown that all these degradations have to be corrected

Received Oct. 18, 2006; revision accepted Dec. 15, 2006.
For correspondence or reprints contact: Jianbin Xiao, STR 5.203, University Medical Center Utrecht, Universiteitsweg 100, 3584 CG Utrecht, The Netherlands.
E-mail: j.xiao@azu.nl
COPYRIGHT © 2007 by the Society of Nuclear Medicine, Inc.

Downloaded from jnm.snmjournals.org by on March 15, 2017. For personal use only.

for to optimize clinical SPECT images (*4–9*). The correction of attenuation and camera blurring is a relatively straightforward and well-established process. Accurate modeling of scatter is, however, complex because of the highly nonuniform density of thoraxes, variation in thorax dimensions, additional attenuation and scatter caused by female patients' breasts, and the complicated spectrum of ^{201}Tl, which consists of multiple photopeaks. Unfortunately, scattered photons cannot simply be neglected because they account for 50% of the total amount of detected photons for a typical ^{201}Tl cardiac SPECT study (*10,11*). Several authors have proposed various approximate, spatially variant models for scatter correction in iterative SPECT reconstruction (*10, 12–16*). Most of these models perform well for uniform objects and with isotopes such as ^{99m}Tc (140 keV) but are less suitable for highly nonuniform media such as the thorax or for lower-energy isotopes such as ^{201}Tl (72 keV). Monte Carlo–based scatter correction, on the other hand, is a more general and accurate correction method. Because of a prohibitively long computation time and huge memory requirement, fully 3-dimensional (3D) Monte Carlo–based statistical reconstruction has only recently become feasible. Our group has developed an accelerated Monte Carlo–based, fully 3D statistical reconstruction system (*17*). For a typical cardiac acquisition consisting of 64 projections with 64 × 64 binned data, our method can complete a reconstruction (15 iterations with 8 subsets) within a couple of minutes on a stand-alone personal computer with a dual central processing unit (2.66 GHz) (*18*).

Previously, we evaluated 3D Monte Carlo–based scatter correction for ^{99m}Tc imaging (*19*) and found moderate improvement in several image-quality metrics over triple-energy-window scatter correction and a method that does not correct for scatter. However, much more scatter needs correcting in ^{201}Tl imaging than in ^{99m}Tc imaging (*10,11*). In addition, triple-energy-window correction is not suitable for the complicated spectrum of ^{201}Tl. Other window-based scatter reduction methods require many energy windows, which often are not available. We therefore hypothesized that the Monte Carlo–based scatter correction could be an attractive option for ^{201}Tl SPECT. Thus, our goal was to evaluate the effectiveness of 3D Monte Carlo–based scatter correction in ^{201}Tl imaging. To this end, a series of physical phantom experiments, which represented a variety of realistic anatomic configurations, was performed. Statistical reconstruction including Monte Carlo–based scatter correction was compared with reconstruction methods that do not correct for scatter. We assessed the noise properties of Monte Carlo–based scatter correction, the robustness of this approach to anatomic variations, the contrast separability of perfusion defects, and the uniformity.

MATERIALS AND METHODS

Phantom Configurations

Four clinically realistic phantom configurations (Data Spectrum Corp.) were used for our evaluation: a large anthropomorphic thorax (model ECT/TOR/P), and a small anthropomorphic thorax (model ECT/LUNG/P), each with breasts (model ECT/SOL-BR/M) and without breasts (Fig. 1). The lateral and anteroposterior dimensions were 38 and 26 cm, respectively, for the large phantom and 32 and 24 cm, respectively, for the small phantom. Each phantom configuration comprised a cardiac insert (model ECT/CAR/I) representing the left ventricle, 2 lung inserts, a liver insert, and a spine insert. Two solid defects (2 mL each) were placed in the anterior and inferior walls of the cardiac insert. These 4 phantom configurations were also used without solid defects for the nondefect studies. The same configurations had been used in our recent publication about scatter correction for ^{99m}Tc SPECT (*19*).

The relative activity concentration ratio myocardium:liver:lungs:background was 43:19:1:2, which reflects the distributions encountered in clinical ^{201}Tl studies (*20,21*). Absolute activities in the myocardium were based on 3% uptake for 148 MBq of ^{201}Tl.

Measurements

The measurements were performed using a dual-head camera (ADAC Vertex; Philips) equipped with extra-high-resolution collimators (Vantage; Philips) and with 2 scanning line sources containing approximately 5.5 GBq of ^{153}Gd each. A 180° study for simultaneous transmission and emission scans was acquired in 64 projections. Projections were acquired from right anterior oblique (–45°) to left posterior oblique (+135°). To assess the noise properties of various reconstruction algorithms, we generated 10 noise realizations from a high-count emission scan. The acquisition time of this high-count emission scan was 4,000 s per projection, which is 100 times longer than for a normal clinical scan. The projections we obtained can therefore be regarded as containing a negligible amount of noise. To create realistic count levels, the almost noise-free projection data were downscaled by a factor of 100. For the dual-head system used here, this count level corresponds to a clinically realistic total acquisition time of 21.3 min. A set of noise realizations of projection data was generated by adding Poisson noise (*22*) to the scaled projections. A different random seed was used for each noise realization.

The ^{201}Tl emission data were measured in the low and high ^{201}Tl photopeak windows (72 keV ± 10% and 167 keV ± 10%)

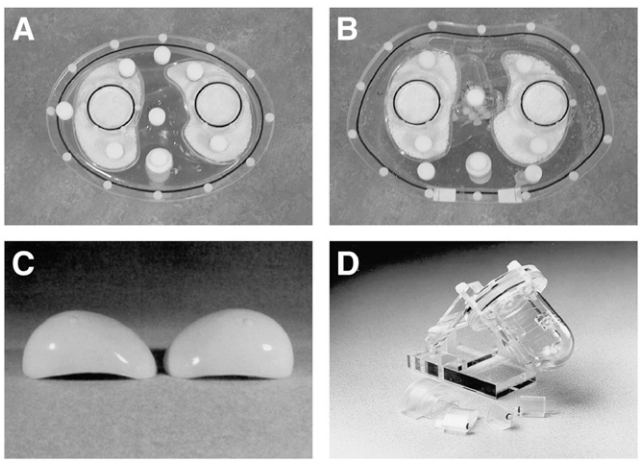

FIGURE 1. Photographs of the phantoms: small thorax (A), large thorax (B), breast attachments (C), and myocardial insert with solid defect set (D). (Images courtesy of Data Spectrum Corp.)

Downloaded from jnm.snmjournals.org by on March 15, 2017. For personal use only.

and then summed. During emission acquisitions, transmission data were collected in a 20% wide energy window centered at 100 keV inside a moving electronic window. The acquisition time was 39 s per projection. To correct for the downscatter of ^{201}Tl γ-photons into the 100-keV transmission window, we used a 100-keV scatter window (100 keV ± 10%) covering the detector area outside the moving electronic window. The acquisition matrix was 128 × 128 with a pixel size of 4.72 mm for both emission and transmission data.

Image Reconstruction

Image reconstructions using ordered-subset expectation maximization (OS-EM) (*23*) algorithms with 3 different types of photon transport modeling were compared. In the first method (the A [i.e., attenuation] method), nonuniform attenuation correction was incorporated into the OS-EM method. Attenuation maps were used to perform nonuniform attenuation correction. The second method (the AD [i.e., attenuation and detector response] method) modeled both attenuation correction and detector response (collimator and detector blurring) during the reconstruction. We used precalculated point-spread function tables that describe the gaussian distance-dependent detector response of a point source in air. The full width at half maximum of the gaussian kernels was calculated on the basis of the geometric collimator resolution and intrinsic detector resolution (*24*). The third method (the ADS [i.e., attenuation, detector response, and scatter] method) was fully 3D Monte Carlo–based reconstruction performed using dual-matrix OS-EM (*25,26*). Attenuation and detector blurring were modeled in both the forward projection and the backprojection. Monte Carlo simulation of ^{201}Tl self-scatter was, however, used only during calculation of the forward projection (*17*). The Monte Carlo simulator was accelerated using convolution-based forced detection (*24*), with which 10^5 photon paths per subset were found to be sufficient for reconstructions of cardiac perfusion studies (*18*). Seven orders of Compton scatter were generated. Downscatter of ^{201}Tl photons to the ^{153}Gd transmission window was corrected by using a scatter window. We elaborate on the issue of downscattered ^{153}Gd photons to the 72-keV window in the "Discussion" section.

During OS-EM reconstruction, both resolution and noise increased with each iteration. The resolution of OS-EM reconstruction is also known to vary spatially. In addition, algorithms using different photon transport models have different convergence speeds, which depend on the activity distribution. Because over-iteration followed by postfiltering can lead to more accurate results than does early stopping of the iteration process and ensures highly homogeneous resolution (*27,28*), we used a large number of updates (30 iterations with 8 subsets per iteration) to produce images with high resolution but with a higher noise level than would normally be ideal. Three-dimensional gaussian filters using various kernel sizes were then applied to these images. In this way, we obtained a series of images with a range of noise levels and associated contrast levels, facilitating the generation of contrast-to-noise curves and enabling us to compare the contrasts of postfiltered images obtained with different algorithms at an equal noise level.

Attenuation maps were reconstructed using the ordered-subset convex algorithm (*29*) with 8 subsets and 30 iterations. To reduce noise, we first filtered the attenuation maps using a 3D gaussian kernel (full width at half maximum, 2.5 pixels). Then, median filtering was applied twice using a 3D cubic kernel of 5 × 5 × 5 pixels (*19*).

Accuracy Check of Forward Projector for ADS

To evaluate the point source response calculated by our Monte Carlo simulator, we performed γ-camera measurements with a ^{201}Tl point source in the center of a water-filled cylinder phantom with a radius of 11.1 cm. The distance between the point source and the collimator surface was 12.9 cm. The profiles of the measured and simulated point source responses matched perfectly in both ^{201}Tl photopeak windows (Fig. 2). The same measurements were also performed with the point source in air. The profiles of the measured and simulated responses showed good agreement (Fig. 2).

Assessment of Reconstructed Images

This section describes the qualitative and quantitative methods we used to assess the reconstructed images. Several of these

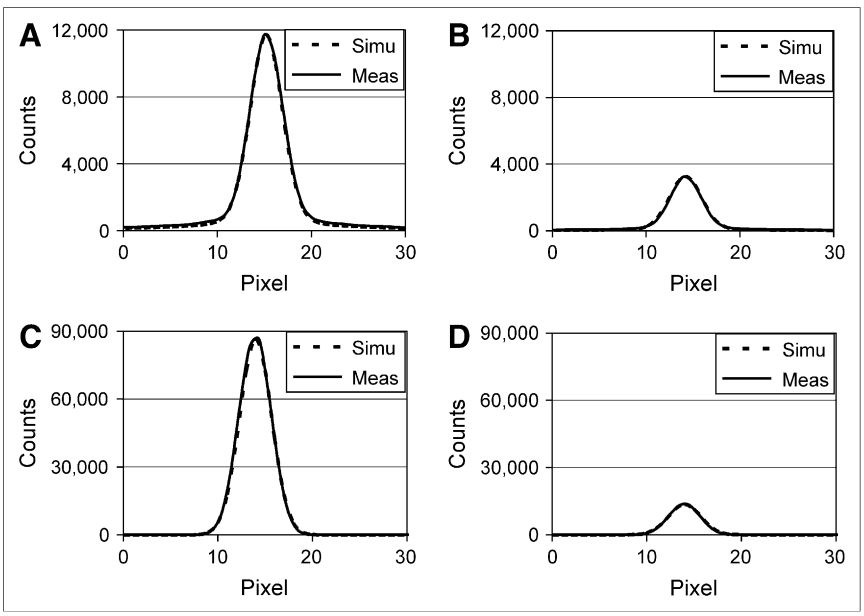

FIGURE 2. Comparisons of measured (Meas) and simulated (Simu) point-spread function tables for water-filled cylinder phantom (A and B) and for air (C and D), for both photopeak windows of ^{201}Tl: 72 keV ± 10% (A and C) and 167 keV ± 10% (B and D).

Downloaded from jnm.snmjournals.org by on March 15, 2017. For personal use only.

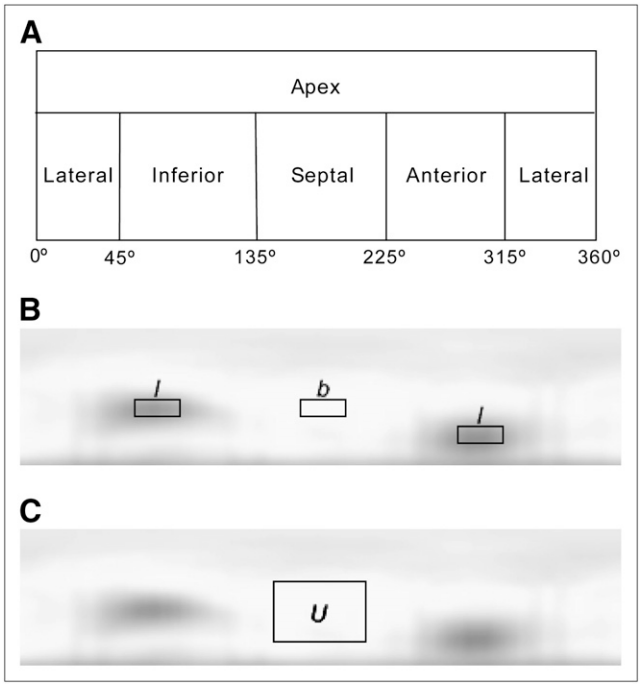

FIGURE 3. Illustrations of spherically sampled apex and cylindrically sampled myocardial wall in circumferential plane (A); locations of the 2 defect regions (l) and background region (b) in circumferential plane (B); and location, in circumferential plane, of uniform region U used for calculating noise (C).

assessment procedures have already been introduced, extensively discussed, and used in a recent publication about scatter correction for ^{99m}Tc myocardial perfusion studies (*19*).

Circumferential Planes. Quantitative analysis was performed using circumferential planes. Such planes are constructed by projecting the maximum-counts circumferential profiles onto a rectangular plane (Fig. 3). The anterior, lateral, inferior, and septal walls of the myocardium were sampled cylindrically, and the apex was sampled spherically (*30,31*).

Contrast. Two types of contrast were used to assess the images: absolute contrast (C_a) and relative contrast (C_r)

$$C_a = |l - b|,\ C_r = \frac{C_a}{b}, \qquad \text{Eq. 1}$$

where *l is* the average pixel value in the 2 cold defects, which are located in the inferior and anterior walls, and *b* is the average pixel value in the background regions beside the defects. The defect and background regions are illustrated in Figure 3. The regions of interest for the defects were 60% of the true defect sizes and were centered at the minimum pixel value within each defect.

Noise Properties. For each phantom configuration, the mean of the circumferential planes of the 10 noise realizations was subtracted from the circumferential plane of each noise realization. We determined the normalized SD in the uniform region U (Fig. 3) in the subtraction image.

$$\text{Normalized SD} = \frac{1}{u}\sqrt{\frac{\sum_{n}^{N}(\tilde{\lambda}(n) - \langle\tilde{\lambda}\rangle)^2}{N-1}}, \qquad \text{Eq. 2}$$

where $\tilde{\lambda}(n)$ is the *n*th pixel value within the region U in the subtraction image, *N* is the total number of pixels in the region, and *u* is the average pixel value of the region U in the circumferential plane of each noise realization.

Contrast Separability of Cold Defects. The detectability index *d* (*19,32*) was used to assess the performance of each reconstruction method in quantitatively distinguishing the myocardium with defects from the myocardium without defects. Relative contrast C_r (Eq. 1) was calculated from both defect and nondefect reconstructions. The contrast values obtained for nondefect studies were due to noise and anatomic variation only and will be referred to as the reference contrast. At a fixed normalized SD level (obtained by 3D gaussian postprocessing filtering using various kernel sizes), both the defect and the nondefect classes contain 40 images (10 noise realizations times 4 different phantom configurations). Within each class, the relative contrasts of images have a certain mean (*M*) and a certain SD. The detectability index *d* is given by:

$$d^2 = \frac{(M_{lc} - M_{rc})^2}{\frac{1}{2}SD_{lc}^2 + \frac{1}{2}SD_{rc}^2}, \qquad \text{Eq. 3}$$

where M_{lc} is the mean of C_r within the defect class, M_{rc} is the mean of C_r within the reference class, SD_{lc} is the SD of C_r within the defect class, and SD_{rc} is the SD of C_r within the reference class.

Robustness. Because the same cardiac insert was used for each phantom configuration, we expected to obtain almost identical cardiac profiles among all the phantom configurations, when all the anatomy-dependent corrections were perfectly performed during reconstruction. Here, we used the robustness (*R*), described elsewhere (*19*), to measure the extent to which anatomic variations influenced the reconstructed myocardium; ideally, they should not exert any influence at all.

Let us first define the circumferential profile $P_i^n(\alpha)$, where *i* labels 1 of the 4 phantom configurations, *n* enumerates 1 of the 10 noise realizations, and α represents the angular sample in the polar coordinate system. $P_i^n(\alpha)$ is a 4-pixel-wide circumferential profile taken from the circumferential plane obtained from a nondefect study. The average of $P_i^n(\alpha)$ over all 4 phantom configurations and all noise realizations is denoted as $\overline{P}(\alpha)$.

The robustness R_i^n is defined as:

$$R_i^n = \frac{\int_{0^0}^{360^0} |P_i^n(\alpha) - \overline{P}(\alpha)| d\alpha}{360\text{AADC}}, \qquad \text{Eq. 4}$$

where the average absolute defect contrast (AADC) is the average of C_a over all 4 phantom configurations with myocardial defects, and the integration is divided by 360 because the integration is performed by summing 360 values that are 1° apart. The numerator of Equation 4 is based on nondefect phantom configurations and thus represents the anatomy-induced variations in the cardiac profiles. The robustness compares the strength of these anatomy-induced variations to the contrast induced by true defects (represented by AADC).

Uniformity. For every noise realization, the accuracy of each reconstruction method for the homogeneously perfused myocardium can be assessed by calculating the uniformity:

$$\text{Uniformity}_i^n = \frac{\sigma_{P_i^n(\alpha)}}{\text{AADC}}, \qquad \text{Eq. 5}$$

Downloaded from jnm.snmjournals.org by on March 15, 2017. For personal use only.

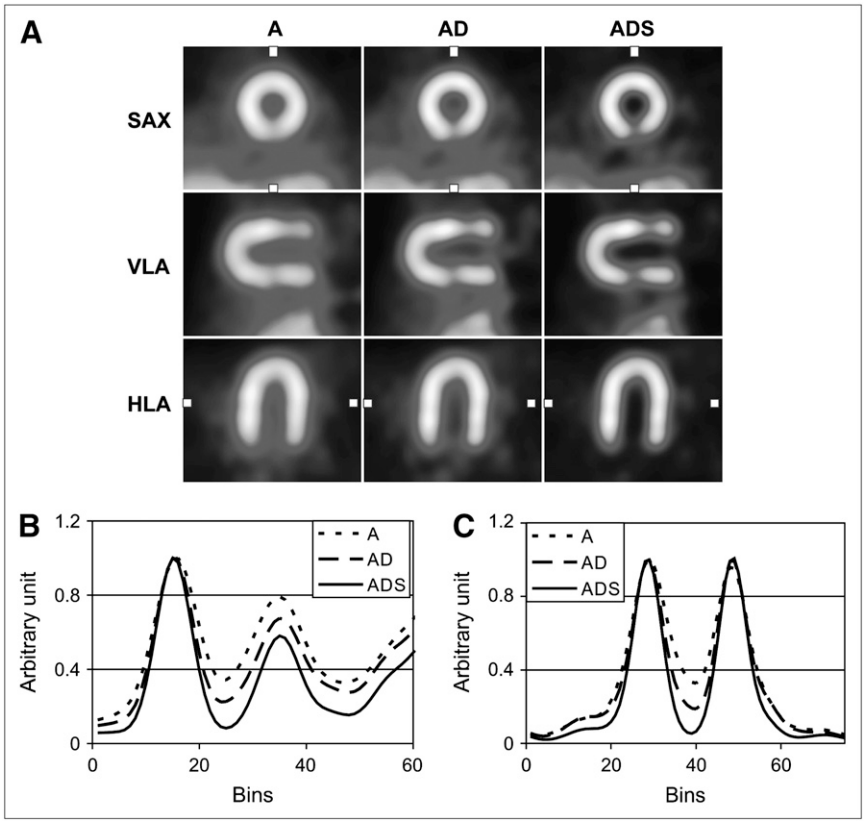

FIGURE 4. (A) Short-axis (SAX) views of reconstructions at typical noise level (normalized SD, 0.1), corresponding vertical long-axis (VLA) views, and corresponding horizontal long-axis (HLA) views. Two solid defects were placed in the anterior and inferior walls. Boxes in SAX and HLA views mark location of profiles. (B and C) Vertical profiles through inferior defect in SAX views (B) and horizontal profiles through uniformly perfused lateral and septal walls in HLA views (C). Each profile was normalized to its maximal pixel value.

where $\sigma_{P_i^n(\alpha)}$ is the SD of $P_i^n(\alpha)$. Uniformity was expected to be equal to zero when all the image-degrading factors were perfectly corrected for during reconstruction.

RESULTS

A typical reconstructed myocardium of the large thorax phantom with breasts is shown for each algorithm in Figure 4 at a noise level for which normalized SD is equal to 0.1. The images at this noise level were regarded by nuclear medicine specialists as having a typical noise level in clinics. Short-axis views, vertical-long-axis views, and horizontal-long-axis views are shown. The ADS images provide better visual defect contrast and less scatter contamination from liver activity than do the A and AD images. Vertical profiles through the inferior defect in the short-axis views confirmed that the ADS algorithm gives better defect contrast than do the other 2 methods. In all axial views and in the profiles, we obtained a better contrast between the myocardium and the chambers with the ADS method.

Figure 5 compares contrast-to-noise curves for different reconstruction methods. The noise was varied by changing the kernel size of the 3D gaussian postprocessing filter. For all methods, noise increased with increasing contrast. For each individual phantom configuration, the images reconstructed by the A and AD methods had lower overall contrast when compared at an equal noise level, and had higher noise when compared at an equal contrast level, than did the images reconstructed by the ADS method. The contrast–noise curves in Figure 5 show that the ADS method achieved contrast values that were approximately 10%–24% higher than those obtained with the AD method and 11%–37% higher than those achieved by the A method when compared at an equal noise level. Noise for the ADS method was approximately 27% lower than that for the AD method and 34% lower than that for the A method when comparisons were made at a typical contrast level ($C_r = 0.44$). Figure 6 shows that, for all phantom configurations, the ADS method provided better contrast separability than did the A or AD method.

The robustness of each method at the noise level corresponding to a normalized SD of 0.1 is shown in Table 1. The smaller the value, the more robust (i.e., the less sensitive) was the algorithm to anatomic variations. Therefore, the ADS method was less sensitive to anatomically induced scatter and attenuation than was the A or AD method and clearly outperformed them in terms of robustness and uniformity. The results of the uniformity measurement at the same fixed noise level as was used for the robustness measurement are also shown in Table 1. The ADS method clearly provided a more uniform image of a homogeneously perfused heart than did the other methods.

DISCUSSION

In this study, a fully 3D Monte Carlo–based scatter correction method (the ADS method) was compared with two other methods: one applying attenuation correction and

Downloaded from jnm.snmjournals.org by on March 15, 2017. For personal use only.

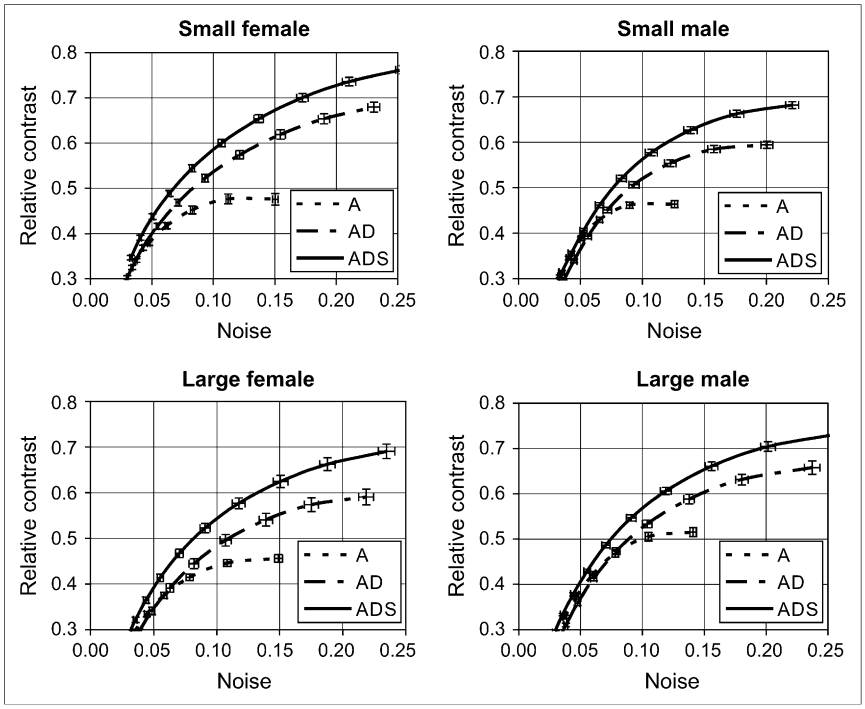

FIGURE 5. Defect contrast as function of noise in myocardium for each phantom configuration and for the 3 reconstruction algorithms. Error bars represent SE for both noise and contrast.

resolution recovery (the AD method) and one applying only attenuation correction (the A method). The ADS method outperformed both of the other methods in terms of contrast-to-noise ratio, contrast separability of cold defects, uniformity, and robustness to anatomic variations. The superiority of the ADS method in these quantitative measures may lead to greater accuracy and sensitivity in the detection of coronary abnormalities, potentially avoiding false-negative diagnoses, with their associated downstream economic and health consequences, and false-positive diagnoses, which unnecessarily expose patients to risky interventions.

The ^{153}Gd photons used to acquire the attenuation map in this work may downscatter into the 72-keV ^{201}Tl photopeak window and deteriorate the accuracy of reconstructed images. To assess the severity of this contamination, we measured the number of ^{153}Gd photons downscattered into the 72-keV emission window for the area of the myocardial envelope in the projection of the large thorax phantom without activity. This number was compared with the number of ^{201}Tl photons for the large thorax phantom with the same absolute activities as were used in this work but without opening the two ^{153}Gd line sources. For all projection angles, the number of ^{153}Gd photons downscattered into the 72-keV window was about 0.6 per pixel in the myocardial envelope. The number of detected ^{201}Tl photons in the 72-keV window was about 22 per pixel on average in the same region. Therefore, the contribution of

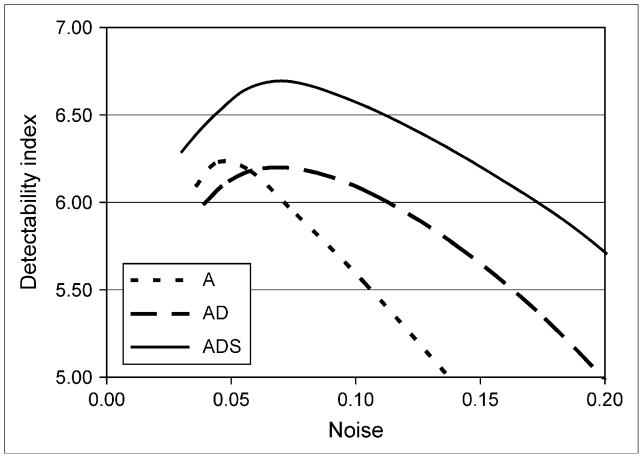

FIGURE 6. Comparison of defect contrast separability for the 3 reconstruction algorithms. Here, we compared which method best differentiated hearts with defects from hearts without defects, for all phantom configurations.

TABLE 1
Uniformity and Robustness Averaged over All Nondefected Phantom Configurations and All Noise Realizations for the 3 Different Methods

Parameter	The A method	The AD method	The ADS method
Uniformity (normalized SD, 0.1)	0.207 (±0.007)	0.209 (±0.007)	0.190 (±0.006)
Robustness R (normalized SD, 0.1)	0.153 (±0.005)	0.153 (±0.005)	0.136 (±0.004)

Data in parentheses are SDs. For robustness, the smaller the value, the more robust was the algorithm to anatomic variations. Monte Carlo–based reconstruction method (ADS) clearly outperforms the other 2 methods (A and AD) in terms of robustness and uniformity.

Downloaded from jnm.snmjournals.org by on March 15, 2017. For personal use only.

downscattered ^{153}Gd photons to the total detected signal was less than 3%. Our finding agreed well with that of Tan et al. (*33*), who showed that with a moving line source and a synchronously moved electronic window, cross-contamination from ^{153}Gd to the 72-keV ^{201}Tl window is negligible. We therefore neglected this contamination in our work.

No window-based scatter correction methods were included in the comparisons presented in this paper. The simplest of such methods, the triple-energy-window approach, is not particularly well suited to the complicated energy spectrum of ^{201}Tl. More sophisticated methods would require even more energy windows, which may not be available on many SPECT cameras currently used in the clinic. Moreover, the use of additional windows requires ad hoc determination of scaling and associated filter parameters. Those parameters may change for different imaging situations—for example, for varied sizes of thoraxes. Finally, the use of noisy projections from small scatter windows inevitably amplifies noise in the reconstructed images. This is a serious disadvantage for ^{201}Tl imaging, because it already suffers from much worse noise properties than does ^{99m}Tc-based cardiac SPECT.

In our previous work (*19*), we evaluated Monte Carlo–based scatter correction for ^{99m}Tc cardiac perfusion imaging. In that case, in comparison with AD, the use of ADS was found to lead typically to a 14% reduction in image noise when the contrast level was kept fixed. The current study showed that, for ^{201}Tl imaging, significantly more noise is suppressed with Monte Carlo–based scatter correction. Depending on the desired contrast level, noise levels may be 25%–30% lower for ADS than for AD. Because noise levels are known to be higher for ^{201}Tl imaging than for ^{99m}Tc SPECT, the substantial reduction of image noise that can be achieved by using Monte Carlo–based scatter correction may become crucial in diminishing the gap in overall image quality between ^{201}Tl and ^{99m}Tc cardiac SPECT.

CONCLUSION

For ^{201}Tl SPECT, our results indicate that the Monte Carlo–based scatter correction method yields a much better contrast-to-noise ratio than do the 2 methods that do not correct for scatter. The Monte Carlo–based algorithm also produces images with larger quantitative differences between defect and nondefect cases, shows better uniformity, and is less sensitive to anatomic variations. Although further tests in a clinical setting are necessary, our results indicate that Monte Carlo–based scatter correction may be decisive in improving the quality of ^{201}Tl-based cardiac SPECT. It could thus facilitate further use of ^{201}Tl in clinics, despite ongoing competition from other isotopes, such as ^{99m}Tc.

ACKNOWLEDGMENTS

This research was supported by Philips Medical Systems, the Dutch Science and Technology Foundation (STW) (grant UGT.6069), the Dutch Organization for Scientific Research (NWO) (grant 917.36.335), and the Fund for Scientific Research–Flanders (FWO).

REFERENCES

1. Travin MI, Bergmann SR. Assessment of myocardial viability. *Semin Nucl Med.* 2005;35:2–16.
2. Germano G, Erel J, Kiat H, Kavanagh PB, Berman DS. Quantitative LVEF and qualitative regional function from gated thallium-201 perfusion SPECT. *J Nucl Med.* 1997;38:749–754.
3. Kelion AD, Anagnostopoulos C, Harbinson M, Underwood SR, Metcalfe M. British Nuclear Cardiology Society. Myocardial perfusion scintigraphy in the UK: insights from the British Nuclear Cardiology Society Survey 2000. *Heart.* 2005;91(suppl 4):iv2–iv5.
4. Hendel RC, Berman DS, Cullom SJ, et al. Multicenter clinical trial to evaluate the efficacy of correction for photon attenuation and scatter in SPECT myocardial perfusion imaging. *Circulation.* 1999;99:2742–2749.
5. Tsui BM, Frey EC, Zhao X, Lalush DS, Johnston RE, McCartney WH. The importance and implementation of accurate 3D compensation methods for quantitative SPECT. *Phys Med Biol.* 1994;39:509–530.
6. Tsui BM, Frey EC, LaCroix KJ, et al. Quantitative myocardial perfusion SPECT. *J Nucl Cardiol.* 1998;5:507–522.
7. King MA, Xia W, Devries DJ, et al. A Monte Carlo investigation of artifacts caused by liver uptake in single-photon emission computed tomography perfusion imaging with technetium 99m-labeled agents. *J Nucl Cardiol.* 1996;3:18–29.
8. Iida H, Shoji Y, Sugawara S, et al. Design and experimental validation of a quantitative myocardial Tl-201 SPECT system. *IEEE Trans Nucl Sci.* 1999;46:720–726.
9. Narayanan MV, King MA, Pretorius PH, et al. Human-observer receiver-operating-characteristic evaluation of attenuation, scatter, and resolution compensation strategies for (99m)Tc myocardial perfusion imaging. *J Nucl Med.* 2003;44:1725–1734.
10. Kadrmas DJ, Frey EC, Tsui BM. Application of reconstruction-based scatter compensation to thallium-201 SPECT: implementations for reduced reconstructed image noise. *IEEE Trans Med Imaging.* 1998;17:325–333.
11. Hademenos GJ, King MA, Ljungberg M, Zubal IG, Harrell CR. A scatter correction method for Tl-201 images: a Monte-Carlo investigation. *IEEE Trans Nucl Sci.* 1993;40:1179–1186.
12. Frey EC, Ju ZW, Tsui BMW. A fast projector-backprojector pair modeling the asymmetric, spatially varying scatter response function for scatter compensation in SPECT imaging. *IEEE Trans Nucl Sci.* 1993;40:1192–1197.
13. Beekman FJ, Eijkman EGJ, Viergever MA, Borm GF, Slijpen ETP. Object shape dependent PSF model for SPECT imaging. *IEEE Trans Nucl Sci.* 1993;40:31–39.
14. Beekman FJ, den Harder JM, Viergever MA, vanRijk PP. SPECT scatter modelling in non-uniform attenuating objects. *Phys Med Biol.* 1997;42:1133–1142.
15. Meikle SR, Hutton BF, Bailey DL. A transmission-dependent method for scatter correction in SPECT. *J Nucl Med.* 1994;35:360–367.
16. Walrand SH, van Elmbt LR, Pauwels S. Quantitation in SPECT using an effective model of the scattering. *Phys Med Biol.* 1994;39:719–734.
17. Beekman FJ, De Jong HW, van Geloven S. Efficient fully 3-D iterative SPECT reconstruction with Monte Carlo-based scatter compensation. *IEEE Trans Med Imaging.* 2002;21:867–877.
18. De Wit TC, Xiao J, Beekman FJ. Monte Carlo-based statistical SPECT reconstruction: influence of number of photon tracks. *IEEE Trans Nucl Sci.* 2005;52:1365–1369.
19. Xiao J, de Wit TC, Staelens SG, Beekman FJ. Evaluation of 3D Monte-Carlo Based Scatter Correction for Tc-99m Cardiac Perfusion SPECT. *J Nucl Med.* 2006;47:1662–1669.
20. LaCroix KJ, Tsui BM, Hasegawa BH. A comparison of 180 degrees and 360 degrees acquisition for attenuation-compensated thallium-201 SPECT images. *J Nucl Med.* 1998;39:562–574.
21. Kadrmas DJ, Frey EC, Tsui BM. Simultaneous technetium-99m/thallium-201 SPECT imaging with model-based compensation for cross-contaminating effects. *Phys Med Biol.* 1999;44:1843–1860.
22. Press WH, Flannery BP, Teukolsky SA, Vetterling WT. *Numerical Recipes in C: The Art of Scientific Computing*. 2nd ed. New York, NY: Cambridge University Press; 1992.
23. Hudson HM, Larkin RS. Accelerated image-reconstruction using ordered subsets of projection data. *IEEE Trans Med Imaging.* 1994;13:601–609.

Downloaded from jnm.snmjournals.org by on March 15, 2017. For personal use only.

24. De Jong HWAM, Slijpen ETP, Beekman FJ. Acceleration of Monte Carlo SPECT simulation using convolution-based forced detection. *IEEE Trans Nucl Sci.* 2001;48:58–64.
25. Kamphuis C, Beekman FJ, Van Rijk PP, Viergever MA. Dual matrix ordered subsets reconstruction for accelerated 3D scatter compensation in single-photon emission tomography. *Eur J Nucl Med.* 1998;25:8–18.
26. Kadrmas DJ, Frey EC, Karimi SS, Tsui BMW. Fast implementations of reconstruction-based scatter compensation in fully 3D SPECT image reconstruction. *Phys Med Biol.* 1998;43:857–873.
27. Miller TR, Wallis JW. Clinically important characteristics of maximum-likelihood reconstruction. *J Nucl Med.* 1992;33:1678–1684.
28. Beekman FJ, Slijpen ET, Niessen WJ. Selection of task-dependent diffusion filters for the post-processing of SPECT images. *Phys Med Biol.* 1998;43:1713–1730.
29. Kamphuis C, Beekman FJ. Accelerated iterative transmission CT reconstruction using an ordered subsets convex algorithm. *IEEE Trans Med Imaging.* 1998;17:1101–1105.
30. Germano G, Kavanagh PB, Waechter P, et al. A new algorithm for the quantitation of myocardial perfusion SPECT. I: Technical principles and reproducibility. *J Nucl Med.* 2000;41:712–719.
31. de Puey EG, Garcia EV, Berman DS. *Cardiac SPECT Imaging*. 2nd ed. Philadelphia, PA: Lippincott Williams and Wilkins; 2001.
32. Barrett HH. Objective assessment of image quality: effects of quantum noise and object variability. *J Opt Soc Am A.* 1990;7:1266–1278.
33. Tan P, Bailey DL, Meikle SR, Eberl S, Fulton RR, Hutton BF. A scanning line source for simultaneous emission and transmission measurements in SPECT. *J Nucl Med.* 1993;34:1752–1760.

Downloaded from jnm.snmjournals.org by on March 15, 2017. For personal use only.

The Journal of NUCLEAR MEDICINE

Evaluation of 3D Monte Carlo–Based Scatter Correction for ^{201}Tl Cardiac Perfusion SPECT

Jianbin Xiao, Tim C. de Wit, Wojciech Zbijewski, Steven G. Staelens and Freek J. Beekman

J Nucl Med. 2007;48:637-644.
Doi: 10.2967/jnumed.106.037259

This article and updated information are available at:
http://jnm.snmjournals.org/content/48/4/637

Information about reproducing figures, tables, or other portions of this article can be found online at:
http://jnm.snmjournals.org/site/misc/permission.xhtml

Information about subscriptions to JNM can be found at:
http://jnm.snmjournals.org/site/subscriptions/online.xhtml

The Journal of Nuclear Medicine is published monthly.
SNMMI | Society of Nuclear Medicine and Molecular Imaging
1850 Samuel Morse Drive, Reston, VA 20190.
(Print ISSN: 0161-5505, Online ISSN: 2159-662X)

© Copyright 2007 SNMMI; all rights reserved.

SNMMI SOCIETY OF NUCLEAR MEDICINE AND MOLECULAR IMAGING